Hydrogeophysical characterization and determination of petrophysical parameters by integrating geophysical and hydrogeological data at the limestone vadose zone of the Beauce aquifer

Mohamad Abbas, Jacques Deparis, Arnaud Isch, Céline Mallet, Clara Jodry, Mohamed Azaroual, Bouamama Abbar, Jean-Michel Baltassat

Journal Pre-proofs

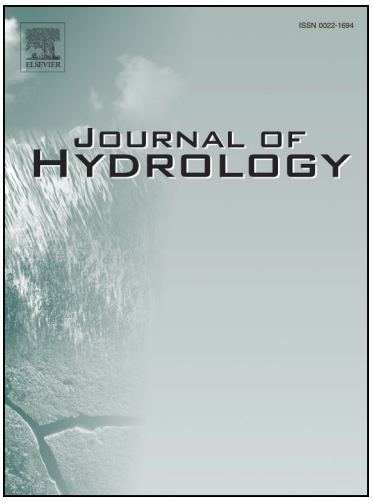

Research papers

Hydrogeophysical characterization and determination of petrophysical parameters by integrating geophysical and hydrogeological data at the limestone vadose zone of the Beauce aquifer

M. Abbas, J. Deparis, A. Isch, C. Mallet, C. Jodry, M. Azaroual, B. Abbar, J.M. Baltassat

PII: S0022-1694(22)01295-1
DOI: https://doi.org/10.1016/j.jhydrol.2022.128725
Reference: HYDROL 128725

To appear in: *Journal of Hydrology*

Received Date: 15 February 2022
Revised Date: 10 October 2022
Accepted Date: 11 October 2022

Please cite this article as: Abbas, M., Deparis, J., Isch, A., Mallet, C., Jodry, C., Azaroual, M., Abbar, B., Baltassat, J.M., Hydrogeophysical characterization and determination of petrophysical parameters by integrating geophysical and hydrogeological data at the limestone vadose zone of the Beauce aquifer, *Journal of Hydrology* (2022), doi: https://doi.org/10.1016/j.jhydrol.2022.128725

Hydrogeophysical characterization and determination of petrophysical parameters by integrating geophysical and hydrogeological data at the limestone vadose zone of the Beauce aquifer

M. Abbas[1 *], J. Deparis[2], A. Isch[1], C. Mallet[1], C. Jodry[3], M. Azaroual[1,2] , B. Abbar[1], and J. M. Baltassat[2]

[1] Univ. Orléans, CNRS, BRGM, ISTO, UMR 7327, F-45071, Orléans, France.

[2] BRGM, French Geological Survey, 45060 Orléans, France.

[3] UNISTRA, Azerbaijan State Oil and Industry University, French Azerbaijani University, Baku, Azerbaijan.

*Corresponding Author (abbas_mohammad@live.com)

Abstract

The hydrological characterization of the vadose zone remains a major challenge considering the spatiotemporal variability of its properties and the limitations associated with hydrological measurements techniques. Geophysical methods, in particular the DC-resistivity and ground penetrating radar, can provide large scale images of hydrogeological structures and a non-invasive assessment of the subsurface dynamic processes. However, these approaches rely on the accuracy of the petrophysical relationships connecting the geophysical parameters to hydrogeological ones, where the site-specific determination of the associated petrophysical parameters is considered crucial. The first objective of this study was to investigate the relationship between the water content, geological properties, and geophysical attributes at the vadose zone of a vulnerable limestone aquifer. The second objective aimed to obtain the Archie's and Complex Refractive Index Model (CRIM) petrophysical parameters by using borehole electrical resistivity and cross-hole ground penetrating radar data. For this purpose, we adopted a grid search inversion algorithm where the field geophysical data were integrated with water content profiles simulated by using HYDRUS-1D. The vadose zone profile was divided into three layers, and the inversion was carried out for the petrophysical parameters in each of the model layers. The electrical resistivity and relative dielectric permittivity data showed a very good correspondence with the simulated and experimental water content distributions along the vadose zone profile. The petrophysical parameters estimated by the inversion showed values that fall in the ranges reported in the literature. Similar values have been observed in the different model layers, with slight differences that were attributed to the vertical heterogeneities associated with the alteration and fracturation features of the limestone vadose zone. This study showed a very good correlation between geophysical, hydrogeological and geological data, and highlighted the presence of heterogeneities that can have profound effects on the vadose zone water dynamics.

Key Words: Electrical Resistivity, Ground Penetrating Radar, Archie, Complex Refractive Index Model, Water Content.

1. Introduction

Improved understanding of water flow and transport processes in the vadose zone (VZ) is crucial, considering the critical role this compartment of the subsurface plays within the biosphere and in the transmission of water and contaminants from the surface to the groundwater. Contamination sources mainly originate in the VZ where the transfer of contaminants is impacted by the medium heterogeneities (e.g., fractures, induced preferential flow and rapid infiltration), and by interactions involving a complex interplay between coupled physical, geochemical, and microbial processes (Arora et al., 2019; Stephens, 2019; Nimmo, 2005). Therefore, a better knowledge of the hydrogeological processes and water content distribution within the VZ is essential to protect groundwater resources.

Conventionally, water content measurements were carried out by single-point techniques, such as time domain reflectometry (TDR) or neutron probes (He et al., 2021; Isch et al., 2019; Skierucha et al., 2012; Evett, 2008; Verhoef et al., 2006; Evett, 2003). Advancements in these techniques (e.g., multi-TDR systems) provided the possibility of time-lapse water content monitoring and eventual preferential flow paths detection (Herkelrath et al., 1991). However, such measurements are intrusive, limited to very shallow depths, and provide restricted information at only a series of point locations. These measurements are often not representative of the field scale spatial water content distribution (Robinson et al., 2003). The difficulties involved in obtaining 2-D or 3-D hydrologic images by exploiting such sparse local data introduced geophysical methods as alternative ways of monitoring water content distribution and water fluxes within the VZ (Binley et al., 2015; Vereecken et al., 2006; Rubin and Hubbard, 2005).

Geophysical methods have shown a great potential in providing large-scale and high spatial resolution images of the subsurface hydrogeological processes (Binley et al., 2015; 2010). Several surface and cross-borehole geophysical methods have been recently used for different hydrological applications. These methods include the ground penetrating radar (GPR) (Dafflon et al., 2011; Lunt et al., 2005; Binley et al., 2001), seismic techniques (Blazevic et al., 2020), electrical resistivity (ER) (Mallet et al., 2021; Johnson et al., 2015; Robinson et al., 2008), self-potential (Abbas et al, 2017; Ahmed et al., 2014; Jardani et al., 2012), induced polarization (Johnson et al., 2010) and nuclear magnetic resonance (Vilhelmsen et al., 2014). Additionally, geophysical methods have been recently used to characterize and quantify processes and interactions in the soil–rhizosphere–atmosphere agricultural ecosystem continuum (Garré et al., 2021).

In particular, the GPR and ER methods have been frequently used to investigate water flow dynamics and identify hydrodynamic parameters (Klotzsche et al., 2019, 2018; Paz et al., 2017; Binley et al., 2015). Thanks to well-established petrophysical relationships between water content and both electrical resistivity (e.g., Archie, 1942) and dielectric permittivity (e.g., Topp et al., 1980) of porous media, these methods can provide valuable information on water flow that can be used to parameterize and constrain hydrogeological models. Relative variations of water content distribution in VZ profiles have been successfully estimated by GPR and ER data. These observations were used to monitor infiltration experiments and visualize flow patterns, quantify petrophysical parameters, characterize preferential flow pathways in fractured media (De Jong et al., 2020; Gance et al., 2016; Wehrer and Slater, 2015; Klotzsche et al., 2013; Steelman and Endres, 2011; Brunet et al., 2010; Cassiani et al., 2009b ; Looms et al., 2008; Linde et al., 2006; Kowalsky et al., 2005; Huisman et al., 2003; Binley et al., 2002a; Hubbard et al., 2001a), and even assess the variations of the soil water content associated with root water uptake (Mary et al., 2018; Hagrey, 2007).

Generally, the water content estimates derived from GPR and ER data showed high accuracy and a good reproducibility. However, geophysical methods cannot directly provide water content values. This approach is dependent on the empirical relationships between the sensed physical parameters and the subsurface parameters of interest (e.g., porosity and water saturation), especially in complex heterogeneous mediums such as carbonate environments, which are often characterized by a complex multiple-porosity system consisting of matrix porosity and fissures, vugs, fractures and karst networks (Mallet et al., 2022; Aldana et al., 2021; Ammar and Kamal, 2017; Mount and Comas, 2014 ; Lucia, 2007). Difficulties arise in the need of time-consuming and expensive laboratory calibration of the petrophysical relationships that are basically suitable only for homogeneous formations, and influenced by properties such as the porosity and tortuosity patterns of the medium under study (Mohamed and Hamada, 2017; Glover, 2016). Estimating parameters such as the water content and porosity from geophysical data by using documented literature values of petrophysical parameters can induce a lot of uncertainties in the absence of site-specific calibration. Achieving an efficient determination of site-specific petrophysical parameters is expected to reduce such uncertainties, and can provide a large-scale and time-saving estimation of water content by avoiding destructive and time-consuming hydrogeological measurements and laboratory calibrations.

The presented study is carried out within the framework of the “Observatory of Transfers in the Vadose Zone” (O-ZNS) platform. The general objective of the O-ZNS platform is to investigate the water-rock-biosphere interactions and their associated mass and heat transfer processes in the VZ. This can provide a better understanding of the VZ dynamics and coupled processes by providing physical, biogeochemical and spatially resolved hydrodynamic parameters capable of characterizing water flow patterns and parameterizing transport models. This study first investigates the relationship between geophysical attributes, water content and geological

heterogeneities at the vadose zone of a vulnerable limestone aquifer. An inversion algorithm is then used to obtain the Archie's and CRIM's petrophysical parameters by integrating borehole electrical resistivity and cross-hole ground penetrating radar data with water content profiles simulated by HYDRUS-1D.

2. Study site

2.1. Description

This study was carried out at the O-ZNS observatory, located in the vicinity of the Beauce limestone aquifer at an agricultural site in Villamblain, France (Fig. 1) (DMS coordinates: X = 48°1′5.131″; Y = 1°34′55.333″). The observatory offers a unique experimental setup, composed of an exceptional well having a depth of 20 m and a diameter of 4 m, along with a number of instrumented boreholes and piezometers. Additionally, the observatory will be equipped with innovative complementary environmental sensors such as fiber-optic sensors (e.g., distributed acoustic sensing, distributed temperature sensing), water content monitoring probes (e.g., TDR), and samplers. These sensors can provide quantitative measurements relative to fluid and heat transfer processes within the VZ. During its exploitation, which is planned for several decades, the observatory will allow acquiring original and unique data on the mass (water, solutes, organic and inorganic contaminants, gases, etc.) and heat (induced by temperature gradients, microbiological reactions, etc.) transfer processes across the continuum "Soil-VZ-Capillary Fringe -Aquifer" for environmental issues and water management. A detailed description of the observatory instrumentation setup can be found in Abbar et al. (2021).

2.2. Geology

Direct observations of undisturbed cores complemented with optical log imagery revealed significant vertical and lateral lithological heterogeneities within the VZ units. Three main lithological units have been identified by the direct core observations (Fig. 1): (1) A first top

soil unit having a thickness ranging between 0.9 and 1.8 m, and a silt loam texture referred to as a Hypereutric Cambisol (IUSS Working Group WRB, 2015); (2) a second unit characterized by highly heterogeneous and altered (i.e., fractures, weathering, oxidation) incoherent limestone facies reaching a depth of around 7 m; and (3) a third unit of hard limestone rock (Pithiviers limestone) extending from a depth of around 7 m down to 20 m with a clear evolution of alteration, fracturation and karstification with depth. The water table had an average depth ranging between 16.5 m and 20.5 m over the last decade, with observed historical variations ranging between 14.5 m and 22.5 m since 1966 (Isch et al., 2022).

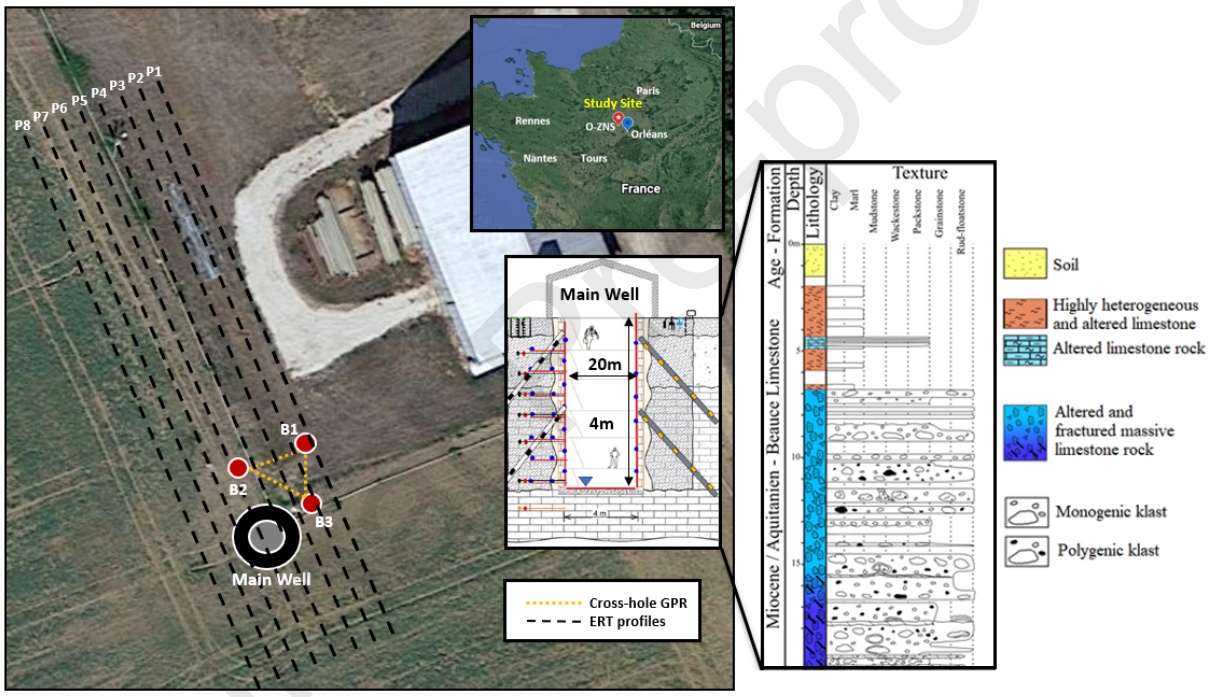

Fig. 1. Study site location, instrumentation, geology and geophysical measurements setup. The figure only shows the boreholes used for this study, several other boreholes surrounding the main well are present at the study site.

3. Methods

3.1. Geophysical data acquisition

168 The O-ZNS infrastructure allows the combination of different geophysical methods and focuses
169 on integrating borehole, cross-hole and surface geophysical techniques that are sensitive to
170 transfer and flow processes. In this section, we present the acquisition protocols of the electrical
171 resistivity tomography (ERT), borehole ER and cross-hole GPR data used in this study.

172 **3.1.1. Electrical Resistivity**

173 A total of 8 ERT profiles were acquired on the 18th of April, 2019 by using a Syscal-Pro 96
174 resistivity meter (Iris Instruments, France) connected to a Syscal Switch Pro 96. The profiles
175 had 48 electrodes each, with an inter-profile spacing of 5 m (Fig. 1). A 2.5 m electrodes spacing
176 was chosen in order to ensure both, an acceptable resolution, and a maximum investigation
177 depth of about 23 m. The measurements were acquired in Dipole-Dipole and Wenner-
178 Schlumberger configurations. Basic filtering steps have been conducted on the acquired ERT
179 profiles (e.g., exterminating bad data points). The profiles were then inverted by Res2Dinv
180 (Loke and Barker,1996) that uses a smoothness-constrained Gauss-Newton least-squares
181 inversion technique to obtain a 2D electrical resistivity model of the subsurface from the field
182 apparent resistivity data (Griffiths and Barker, 1993). The result is a 2D smoothness-constrained
183 distribution of electrical resistivity in the VZ. The effect of temperature variations was
184 considered negligible on the electrical resistivity data along the first 20 meters of the subsurface.
185 This was assumed due to the observed low variations of temperature as a function of depth in
186 the VZ at this time of the year.

187 On the other hand, the ER borehole data were obtained from three different boreholes logs (B1,
188 B2 and B3, cf. Fig. 1) on the 23rd of March, 2017 by means of the dual induction-laterolog
189 (DIL) method. This method consists of focused electrical measurements that rely on transmitter
190 and receiver coils. The measurements are based on an alternating current that generate eddy
191 currents which in turn produce a secondary electromagnetic field. The latter induces an
192 alternating voltage proportional to the formation electrical conductivity in the receiver coil. The

transmitter-receiver pair which uses a low frequency is designed to minimize the effects of the borehole and optimize the depth of investigation and the measurement vertical resolution. A measurement point spacing of 2 cm was used, with a maximum penetration depth varying between 18 m and 19 m depending on each of the borehole's maximum accessible depth.

3.1.2. Ground Penetrating Radar

The cross-hole GPR measurements were acquired by using a ProEx GPR system (Malå Geosciences) on the 24th of January, 2019. The measurements were done by using 100 MHz borehole antennae with a sampling frequency of 1000 MHz and a measurement period of 240 ns. Zero offset profiles (ZOP) were acquired between the three boreholes B1, B2 and B3 (TXB2_RXB1, TXB1_RXB3 and TXB2_RXB3) (Fig. 1). The ZOP method is a commonly used approach for borehole GPR acquisition surveys (Klotzsche et al., 2019). Throughout the ZOP measurements, the transmitting (Tx) and receiving (Rx) antennas are moved simultaneously in two different boreholes with a fixed step size. To conduct the ZOP measurements, the antenna were first pushed to the bottom of each of the boreholes where the maximum accessible depth was 18.98 m (water table). The antennae were then pulled simultaneously towards the surface by using a 0.5 m fixed step size.

One-dimensional velocity profiles were then determined by a standard ray-based analysis approach. For simplicity, the medium was assumed to have no horizontal variation of velocity while obtaining the one-dimensional velocity profiles. After picking the first arrivals (in ReflexW©), the arrival time (t) and the distance between the boreholes were used to determine the GPR electromagnetic wave velocity (v) through the following equation:

$$v = \left(\frac{d}{t - T_0}\right), \quad (1)$$

where T_0 is the time-zero offset, which was obtained by conducting multi-offset measurements with the antenna in free-space. In low-loss and non-magnetic material such as carbonate

formations (e.g., limestone), the relative dielectric permittivity (ε_r) can be then determined at different depths by using the following equation:

$$\varepsilon_r = (c/v)^2, \quad (2)$$

where c is the velocity of an electromagnetic wave in vacuum (~0.3 m/ns). Relative dielectric permittivity profiles were then determined from the obtained velocity profiles by using Eq. 2.

3.2. Hydraulic properties measurements and simulation of water flow within the VZ

3.2.1. Hydraulic properties of the vadose zone samples

Fifteen undisturbed samples representative of the VZ (0-20 m deep) were chosen according to the lithological observations made from the three cored boreholes B1, B2 and B3 (Isch et al., 2022). The samples included three soil samples (S_A, S_B and S_C), four soft sediments and powdery limestone samples (P_A, P_B, P_C and P_D), two calcareous sand samples (I_A and I_B), and six limestone rock samples (R_A, R_B, R_C, R_D, R_E and R_F). These samples were used to estimate the water retention θ(h) and hydraulic conductivity K(h) curves by applying the multistep outflow method (Aldana et al., 2021). The multistep outflow experiments were conducted by using a triaxial system based on the experimental procedure described by Eching et al. (1994). The hydraulic conductivity was calculated from the outflow data based on the method described by Gardner (1956).

3.2.2. Simulation of water flow in the vadose zone

Simulation of water flow within the VZ was then performed over a 55 years period (1966-2020) on a 23 m deep VZ profile (borehole B2) composed of fifteen layers and reconstituted with the HYDRUS-1D software (Šimůnek et al., 2016). The simulation of water flow was based on the one-dimensional vertical water flow in the VZ described by Richards equation (Richards, 1931):

$$\frac{\partial \theta}{\partial t} = \frac{\partial}{\partial z}\left[K\left(\frac{\partial h}{\partial z} + 1\right)\right] - S, \quad (3)$$

where θ is the volumetric water content (cm^3/cm^3), z is the coordinate along the vertical axis (cm), t is the time, h is the matric head (cm), K is the hydraulic conductivity (cm/d) and S is a sink-source term. The Mualem-Van Genuchten analytical model (MVG) was used for the description of the VZ hydraulic properties. The van Genuchten's expression (van Genuchten, 1980) was used to describe the water retention curve:

$$\theta(h) = \begin{cases} \theta_r + \dfrac{\theta_s - \theta_r}{[1 + |\alpha h|^n]^m} & h < 0 \\ \theta_s & h \geq 0 \end{cases} \quad (4)$$

$$\text{with} \qquad m = 1 - \frac{1}{n} \qquad n > 1,$$

where θ_r and θ_s are the residual and saturated volumetric water content (cm^3/cm^3) respectively. α is an empirical parameter related to the matric head (cm^{-1}), and n is a pore size distribution parameter (-). The statistical pore connection model of Mualem (1976) was then used to predict the hydraulic conductivity from the water retention curve:

$$K(h) = K_s S_e^l \left[1 - (1 - S_e^{\frac{1}{m}})^m\right]^2 \quad (5)$$

$$\text{with} \qquad S_e = \frac{\theta - \theta_r}{\theta_s - \theta_r},$$

where K_s is the saturated hydraulic conductivity (cm/d), S_e is the effective saturation (-) and l is a pore connectivity parameter (-) fixed at the value of 0.5 (Mualem, 1976). The measured water retention and hydraulic conductivity data were fitted to the θ(h) and K(h) curves with the MVG model (Eq. 4 and Eq. 5) by using the RETC software (van Genuchten et al., 1991) to infer the VZ hydraulic properties used in our simulations. The representation of the VZ profile

for B2, the values of experimental and fitted (with RETC) saturated volumetric water content (θ_s) and fitted hydraulic conductivity (K_s, in cm/d) are given in Table 1. Water table level and meteorological data were collected from monitoring stations located at the villages of Poiseaux (4 km from the study site) and Bricy (20 km from the study site) respectively. While the weather conditions at the study site may differ slightly during intense and localized rainy events relative to those observed at the Bricy station, these are however considered to be representative over a period of more than 50 years.

Table 1. (a) Description of the samples considered for the representation of the VZ profile and the simulation of water flow with HYDRUS-1D: depth, description, saturated water content (θ_s), experimental saturated water content ($\theta_{s\text{Exp.}}$), hydraulic conductivity (K_s), α, and n.

Geological Unit	Depth (m)	Sample	Description	θ_s (cm3/cm3)	$\theta_{s\ \text{Exp.}}$ (cm^3/cm^3)	K_s (cm/d)	α cm^{-1}	n (/)
1	0.00-0.30	S_A	Soil	0.4735	0.4864	30.24	0.0242	1.15
	0.31-0.60	S_B	Soil	0.4661	0.4612	53.57	0.0242	1.16
	0.61-0.90	S_C	Soil	0.5002	0.4162	47.52	0.0366	1.16
2	0.91-1.30	P_A	Powdery limestone	0.4511	0.4230	7.31	0.0247	1.17
	1.30-3.50	P_B	Powdery limestone	0.3659	0.3525	0.455	0.0073	1.25
	3.51-4.10	I_A	Calcareous sand	0.3918	0.3775	35.22	0.0715	1.20
	4.11-4.60	P_C	Powdery limestone	0.2969	0.3080	0.143	0.0031	1.22
	4.61-4.90	I_B	Calcareous sand	0.3698	0.4336	285.49	0.1600	1.23
	4.91-5.20	R_A	Altered rock	0.2984	0.3400	5000	0.5156	1.36
	5.21-5.50	I_B	Calcareous sand	0.3698	0.4336	285.49	0.1600	1.23
	5.51-6.60	P_D	Powdery limestone	0.3527	0.3491	0.185	0.0040	1.22
3	6.61-9.00	R_B	Massive rock	0.1547	0.1499	1.32	0.0150	1.16
	9.01-11.20	R_D	Massive rock	0.0949	0.1180	0.402	0.0096	1.17
	11.21-11.40	R_C	Massive rock	0.0504	0.0491	0.0097	0.0014	1.23
	11.41-14.00	R_D	Massive rock	0.0949	0.1180	0.402	0.0096	1.17

	14.01-16.00	R_E	Massive rock	0.1172	0.1333	500	0.1266	1.15
	16.01-19.00	R_F	Massive rock	0.1452	0.1639	500	0.1371	1.19

4. Petrophysical Modeling

4.1. Relative Permittivity

The CRIM is a three-phase dielectric mixing model commonly used to describe the relationship between relative dielectric permittivity and subsurface properties such as water content and porosity (Huisman et., 2003; West et al., 2001; Roth et al., 1990):

$$\varepsilon_r^\alpha = \phi S_w \varepsilon_w^\alpha + (1-\phi)\varepsilon_s^\alpha + \phi(1-S_w)\varepsilon_a^\alpha, \quad (6)$$

where ϕ and S_w are the porosity and water saturation respectively, ε_a is the relative dielectric permittivity of air (given a value of 1), ε_w is the relative dielectric permittivity of water, ε_s is the relative dielectric permittivity of the solid phase, considered as a source of uncertainty to be accounted for when using the CRIM.

Besides the ε_s, the second source of uncertainty to be accounted for is the factor α which describes the orientation of the electrical field with respect to the geological formations' geometry (West et al., 2003; Chan and Knight, 1999; Knoll, 1996; Roth et al., 1990; Birchak et al., 1974).

4.2. Electrical Resistivity

In geological formations characterized by medium to coarse grained sediments, the grain surface conductivity effect can be neglected and the bulk electrical resistivity (ρ_0) can be related to subsurface properties such as porosity and fluid saturation by the following modified form of Archie's equation (Winsauer et al., 1952 ; Archie, 1942):

$$\rho_0 = a\rho_f \phi^{-m} S_w^{-n}, \quad (7)$$

where ρ_f is the fluid or pore water electrical resistivity, a is an empirical constant originally referred to as the tortuosity or lithology constant (Winsauer et al., 1952), m is the cementation exponent which is considered to be influenced by the degree of cementation of the rock fabric (Glover, 2010; 2009), and n is the saturation exponent which is independent of the rock matrix and describes how the pore water is connected (Glover, 2017; Looms et al., 2008a; Hendrickx et al., 2002).

Even though Archie's law does not take the surface conduction into account, it is considered to be applicable if the pore fluid conductivity is largely greater than the surface conduction, especially in the case of low clay content formations such as the limestone rock described within the VZ of our study site (Fig. 1). The need of including the surface conductivity arises when other conducting phases such as clay minerals are present in the rock formation. Therefore, during this study, we applied our approach to the limestone rock facies located at a depth between 6.61 m and 19 m, where geological and mineralogical studies (Aldana et al., 2021) suggested that the surface conduction can be practically neglected.

4.3. Inversion

This study aims to estimate the Archie's and CRIM's parameters that can vary according to the study site conditions, and that are considered as sources of uncertainties in the application of these models for the estimation of water content variations. The numerical approach used in this study is based on a grid search inversion algorithm (Fig. 2). The inversion workflow is based on testing the possible combinations of the petrophysical parameters that can provide the best fit between the measured and simulated data. The estimated data are the electrical resistivity and relative dielectric permittivity values calculated by using the Archie's and CRIM's equations respectively. The ER measured data are the 1D electrical resistivity data

acquired by the borehole's ER measurements, while the dielectric permittivity measured data are those generated from the 1D velocity profiles obtained from the GPR cross-hole measurements. The fit between the measured and calculated data is evaluated through calculating the corresponding root mean square error (RMSE) while the algorithm varies the Archie's (a and m) and CRIM's (α and ε_s) petrophysical parameters to be estimated:

$$\mathrm{RMSE} = \sqrt{\frac{\sum_{i=1}^{N}(x_i - \hat{x}_i)^2}{N}}, \tag{8}$$

where x_i represents the observed data, $\hat{x}_i$ represents the data estimated by the model and N is the total number of data points. The procedure is done separately for the Archie's and CRIM's models. The water content profiles data used to calculate the dielectric permittivity and electrical resistivity in the CRIM's and Archie's equation are those simulated by HYDRUS-1D software. The geophysical data, water content and porosity data used for both models are obtained from the geophysical measurements and hydrogeological model of borehole B2. The fluid resistivity in the Archie's equation is given a value of 510 µS/cm obtained from probes and calibrated by laboratory measurements, while the relative dielectric permittivity of water is assumed to be 79.5 at a temperature of 22.0 °C (Buchner et al., 1999). The model was divided into three layers, and the inversion was carried out for each of the layers separately. This step was done to investigate the effect of geological vertical heterogeneities on the obtained petrophysical parameters. The model discretization and layering were designed according to the geological characteristics and hydrogeological simulations results (see section 5.3.1).

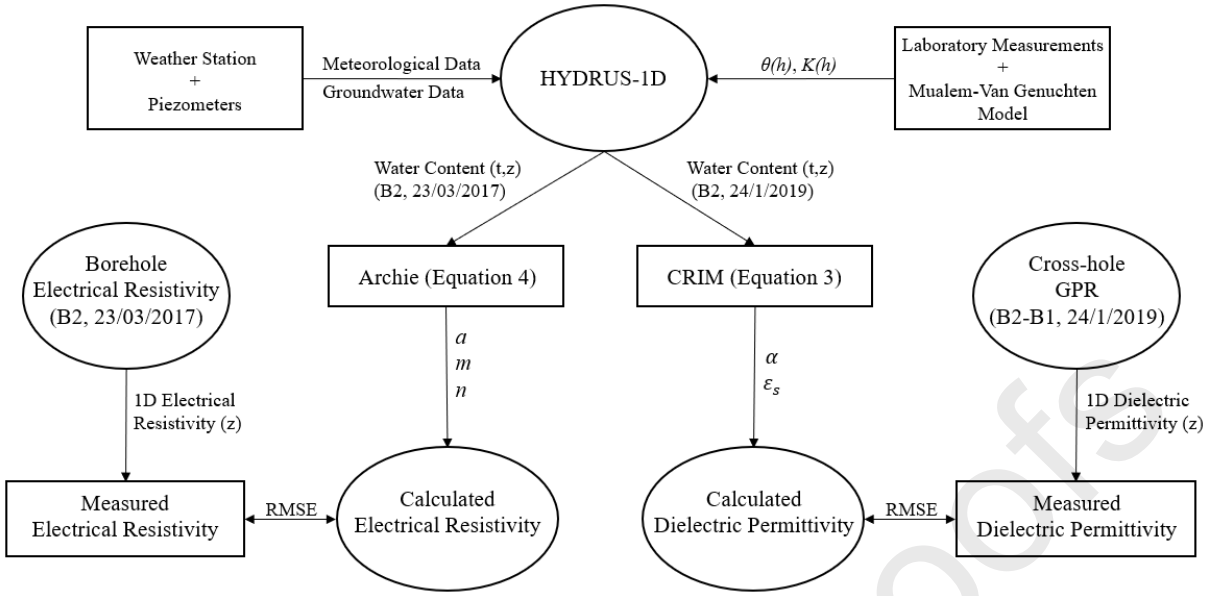

Fig. 2. The inversion algorithm workflow which was done for the Archie and CRIM models separately. The inversion procedure is based on finding the combinations of petrophysical parameters that can provide the best fit between the measured geophysical data and the geophysical profiles calculated by using the water content profiles simulated by HYDRUS-1D.

The results analysis is based on obtaining the combined values of the varied Archie (a and m) and CRIM parameters (α and ε_s) that have the minimal observed RMSE while the algorithm fits the calculated and the measured data. The ranges of variability set for each of the parameters during the inversion were based on common ranges provided in literature for limestone formations. However, the parameters were set to also have values outside these ranges to avoid directing the inversion towards literature values, and to compare our results with those reported in previous studies. Table 1 shows the ranges of the Archie and CRIM parameters used for this inversion and those most commonly reported in the literature for limestone formations. To improve the inversion performance and reduce the different parameters dependencies, the saturation exponent n was fixed to a value of 2 and the calculation was done only for the a and m parameters in the Archie equation. Even though values ranging between 1.4 and 2.5 have been previously given to n in the literature for rocks (e.g., Schön, 2004; Sweeney and Jennings,

339 1960; Rust, 1952), in practice, the saturation exponent is commonly set to 2 for most types of
340 rocks in the absence of laboratory measurements (e.g. Yaramanci et al., 2000; Looms et al.,
341 2008a, 2008b). On the other hand, α was given a range based on its extreme values which are
342 1 and -1. The lower boundary (-1) represents the harmonic arrangement of dielectric
343 components in series, while its upper boundary (1) represents the arithmetic arrangement of
344 dielectric components in parallel (Chan and Knight, 2001;1999).

345 **Table 2** : The ranges of the Archie (a, m and n) and CRIM (α and ε_s) parameters used for the
346 inversion and those commonly reported in the literature for limestone formations.

Model	Parameter	Literature (limestone)	Inversion
Archie	a	$0.2 \leq a \leq 2.3$	$0.1 \leq a \leq 10$
	m	$1.6 \leq m \leq 3$	$1.0 \leq m \leq 10$
	n	$1.5 \leq n \leq 2.5$	$n = 2$
CRIM	α	$-1 \leq \alpha \leq 1$	$-1 \leq \alpha \leq 1$
	ε_s	$4 \leq \varepsilon_s \leq 11$	$1 \leq \varepsilon_s \leq 20$

347 # 5. Results and discussion

348 ## 5.1. Geology

349 Knowing that a strong coherence was observed between the ERT and borehole ER profiles,
350 throughout this work, the ERT profiles are only used for the lithological description and 2-D
351 representation, while the borehole ER data will be used for the water content analysis and as an
352 input in the inversion for its higher resolution (2 cm) and larger number of data points.

353 In correspondence with the geological description, the ERT (profile P2 in Fig. 1) showed three
354 main layers corresponding to the three main geological units shown in Fig. 1 (Fig. 3). The data
355 showed a first low ER unit representing the top soil layer. The latter is followed by a moderate

ER layer down to a depth of around 7 m. This layer corresponds to the incoherent and altered limestone formation. Lateral ER variations (Fig. 3) and dispersed dielectric permittivity values (Fig. 4b) were observed in this layer, which reflects the heterogeneity of this formation. A clear transition zone between the incoherent limestone layer and the underlaying hard limestone rock layer is evident in the relative permittivity and ER data at depths between 6.5 m and 9 m. This is followed by a third relatively higher ER layer corresponding to the massive limestone rock layer. This layer shows lower dielectric permittivity values which started to increase again as the measurements got closer to the water table level (Fig. 4b).

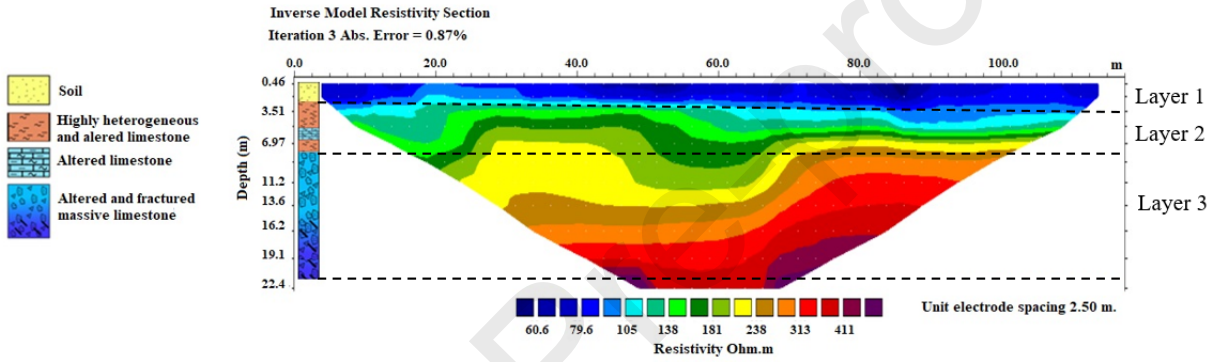

Fig. 3. The 2D smoothness-constrained distribution of electrical resistivity of profile P2. showing 3 main units in accordance with the geology data presented in Fig. 1. All the ERT profiles showed similar results in terms of the lithological structure, therefore, only profile P2 is presented in this work.

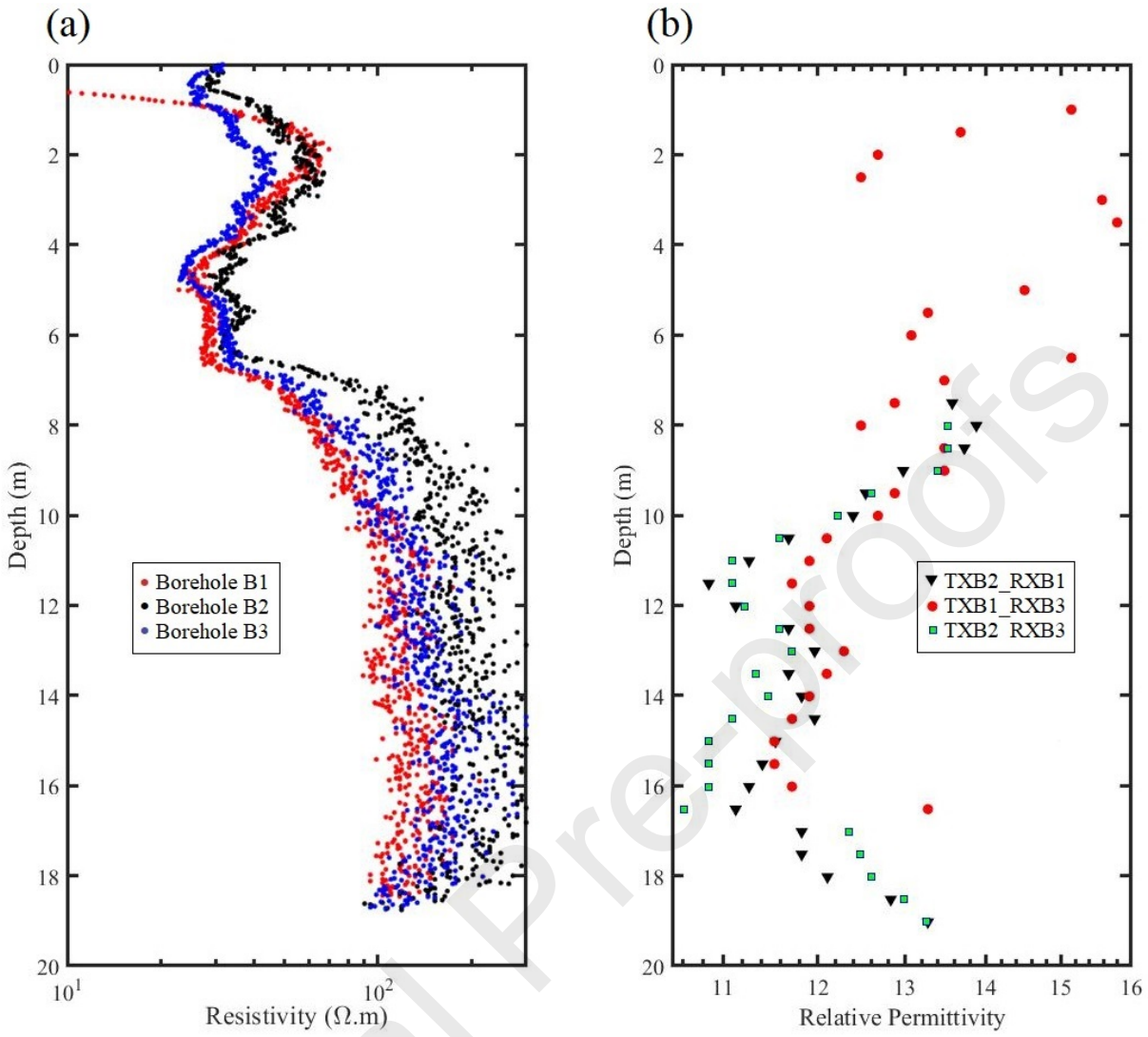

Fig. 4. (a) Electrical resistivity borehole data showing the ER variations in boreholes B1, B2 and B3 (23/03/2017). (b) Relative permittivity results obtained from the cross-hole GPR profiles acquired between boreholes B1, B2 and B3 (24/01/2019).

5.2. Hydrogeology

As shown in Fig. 5, the simulated water content profile obtained by the model for borehole B2 (23/03/2017) showed a good agreement with experimental water content ($R^2 > 0.885$) measured at the same date. This model, which focused on the simulation of the water movement within the matrix components of the VZ, seemed to constitute a first simplified but suitable approach for the unidimensional simulation of water flow within the VZ of the Beauce limestone aquifer.

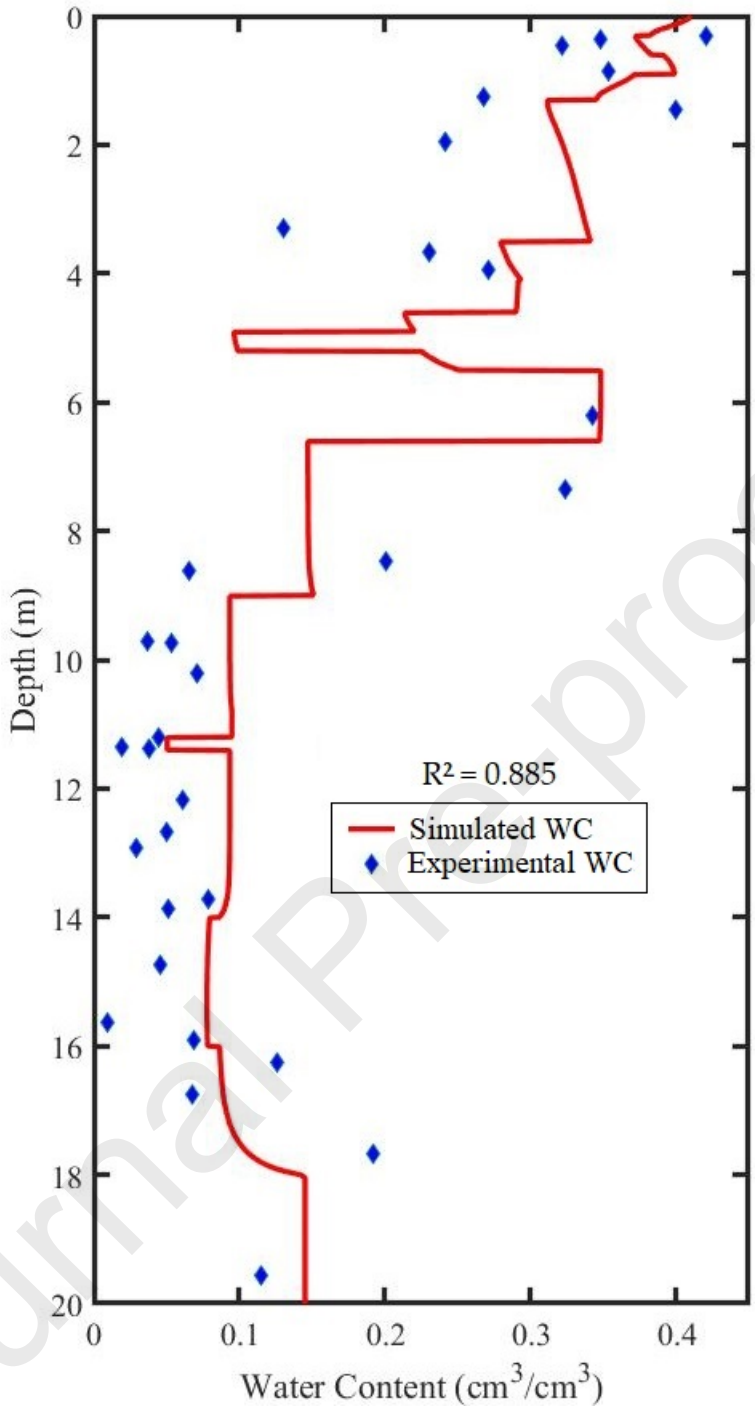

379

380 **Fig. 5** : Experimental water content (WC) plotted against the simulated water content obtained
381 in borehole B2 with the HYDRUS-1D software (23/03/2017).

382 The borehole ER data (23/03/2017) showed a good global correspondence with the simulated
383 water content distribution at the same date (Fig. 6a). This correspondence is characterized with
384 a global increase in the ER values along with the global decrease in the water content. This was

385 followed by a decrease in the ER values with the increase in the water content close to the water
386 table level. Similarly, the relative permittivity data showed a good correspondence with the
387 water content variations (Fig. 6b). A significant coherent decrease in the relative permittivity
388 and water content was observed at a depth between 6.5 m and 9 m located at the transition zone
389 between the incoherent limestone and the hard limestone formations. This was followed by a
390 significant increase in the relative dielectric permittivity values along with the increase in water
391 content close to the water table level. The water content profiles simulated for the dates of the
392 ER (Fig. 6a) and GPR (Fig. 6b) data showed similar values with slight but noticeable
393 differences in the top 6 meters and at a depth between 17 m and 19 m. This was expected
394 knowing that these profiles were simulated for two close periods of the year (23rd of March and
395 24th of January).

396 A similar pattern was observed in the three boreholes ER data and in the three dielectric
397 permittivity profiles, which shows a good repeatability of the field geophysical data. This
398 observation also indicates that the zones around and between the boreholes are globally and
399 relatively homogeneous, despite the presence of local lateral heterogeneities that were observed
400 in each of the geophysical profiles.

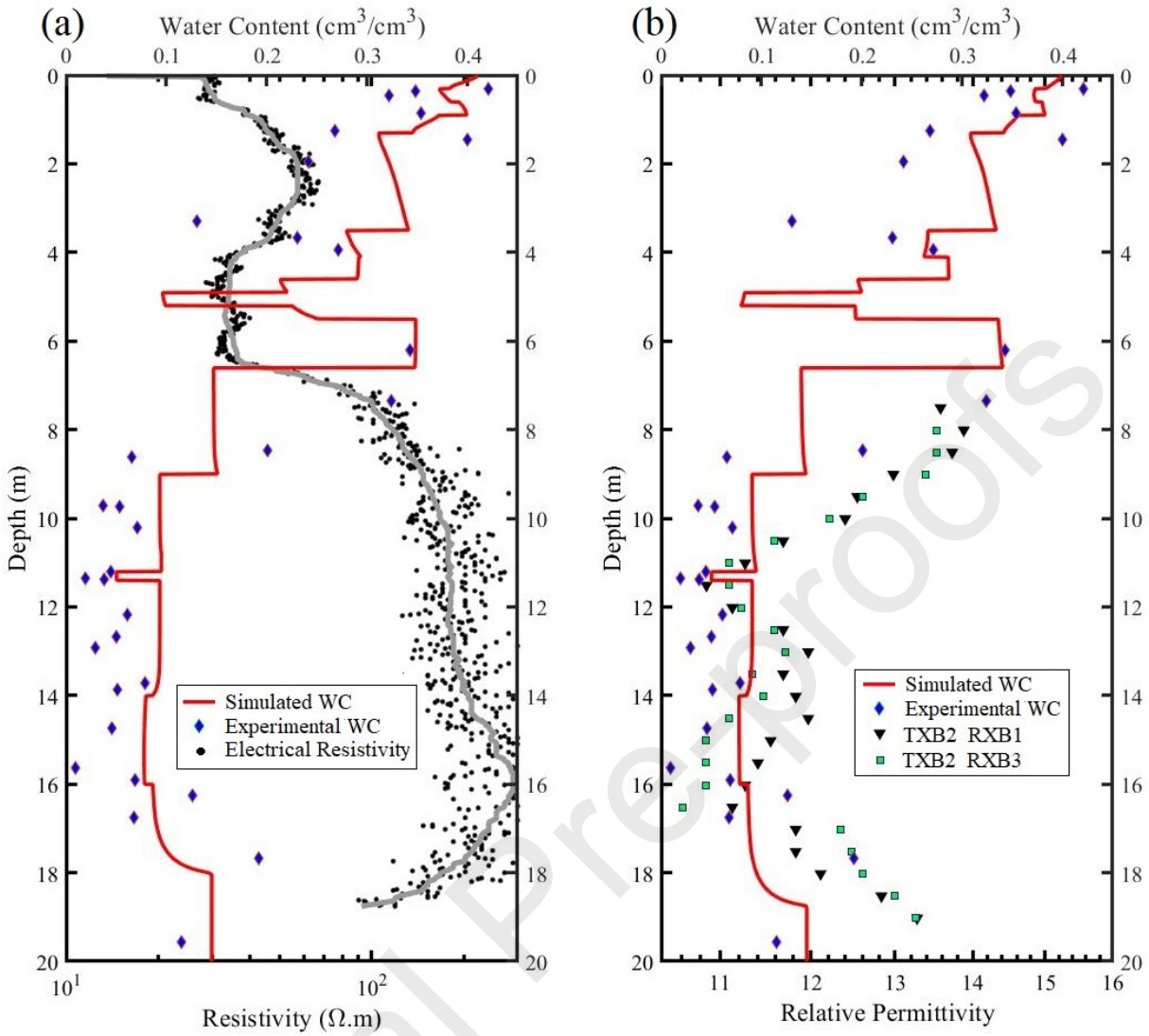

401

402 **Fig. 6. (**a) Borehole ER variations with respect to water content variations simulated by
403 HYDRUS-1D (B2, 23/03/2017), (b) Relative dielectric permittivity distribution obtained from
404 the GPR measurements with respect to water content variations simulated by HYDRUS-1D
405 (B2, 24/01/2019). The water table in borehole B2 had a depth of 18.71 m during the ER
406 measurements and a depth of 18.98 m during the GPR measurements.

407 **5.3. Determination of Petrophysical Parameters**

408 To determine the Archie (a and m) and CRIM (α and ε_s) petrophysical parameters, the measured
409 ER and relative permittivity data and the simulated water content distributions were used in the
410 inversion algorithm described in section 4.3.

5.3.1. Model Structure

As explained previously in section 4.2, the calculation was done for the part of the VZ located at a depth between 6.61 m and 19 m, where the well-cemented microcrystalline texture of the hard limestone rock along with its very low amount of fine-grained material (Aldana et al., 2021) permits the neglection of the grains surface conductivity. Therefore, the inversion model was applied on the geological unit number 3 (Table 1), which was divided into three sub-layers according to lithological description, the hydrogeological model discretization and the water content variations. Layer 1 is located at the top of the unit at a depth between 6.61 m and 9.00 m. This layer, which is considered as the transition zone between the incoherent limestone (P_D) and the massive rock (R_B) materials (Table 1), showed simulated water content variations ranging between 0.147 and 0.151 cm^3/cm^3 (Fig. 5). Layer 2 is located at a depth ranging between 9.01 m and 14.00 m, and is characterized by a limestone rock showing few fissures and slight alterations (R_D) with intercalations of massive limestone rock banks (R_C) (Mallet et al., 2022) which presented a very low porosity (Table 1). Layer 2 showed a simulated water content variation ranging between 0.050 and 0.095 cm^3/cm^3. Layer 3 corresponds to the altered limestone rock that showed a highly heterogeneous structure characterized by an increased evolution towards fracturation and karstification with depth. Layer 3 is located at a depth ranging between 14.01 m and 19 m, and showed the highest water content variation with values ranging between 0.078 and 0.145 cm^3/cm^3. The simulated water content values described here are those obtained for the ER measurements date (23/03/2017), while similar value ranges were also obtained for those of the GPR measurements date (24/01/2019). The inversion was carried out for each of the model's layers separately in order to investigate the effects of vertical heterogeneities on the obtained parameters. This gives us a total of 6 inversions (3 for the CRIM and 3 for the Archie's model).

5.3.2. Inversion Results

436 The inversion results of the Archie's parameters showed a value of 1.60 for the cementation
437 exponent m in Layers 1 and 2 and a value of 1.47 in Layer 3. One can look at the cementation
438 exponent as a measure of connectedness of the pore network which decreases as the m exponent
439 increases (Glover, 2017). Most sediments or sedimentary rock consisting partially or
440 completely of sand-sized fragments have cementation exponents ranging between 1.5 and 2.5
441 (Glover et al., 1997), while lower connectedness and vuggy limestone formations are expected
442 to be represented by higher m values. A wide range of values have been reported in the literature
443 for limestone formations (Worthington, 1993). Values ranging between 1.6 and 2.4 have been
444 reported for carbonates (Schön, 2004; Carothers, 1968; Hill and Milburn, 1956), while it was
445 also suggested that they can also have higher values ranging between 2.5 and 5 due to their
446 poorly connected pore space (Tiab and Donaldson, 2011, 2004). However, knowing that
447 connectedness is a term which also describes the extent to which transport pathways are
448 available, low porosity rocks characterized by relatively direct flow paths due to a well-
449 developed fracture network could have lower values or values close to unity reflecting a fairly
450 good connectedness provided by the fractures network. Therefore, the relatively low values
451 obtained in our study could be related to a well-developed fracture network which is thought to
452 be present in the study site but not fully characterized yet. Even though we used a simple
453 porosity model that doesn't take fractures network into account in the porosity parameter, the
454 relative effect of the fracturation could be reflected in the field resistivity data that have a major
455 influence on the obtained m value during the inversion. Layer 3, which showed a lower m value
456 (1.47) relative to Layers 1 and 2, has a highly heterogeneous structure characterized by
457 increased alteration, fracturation and karstification features relative to the other layers, which
458 might explain the relative decrease of m in this layer. Indeed, complex structural formations
459 have been observed in the limestone VZ at the O-ZNS site (Fig. 7), where fissures, fractures
460 and karst networks were observed at the field scale (Aldana et al., 2021). For example,

millimetric vugs induced by dissolution processes have been observed in the weathered rock formations located at the water table fluctuation zone and corresponding to Layer 3. Further dissolution episodes could have increased the vugs diameters and enhanced the permeability at this layer. As it is evident in the Archie's equation (Eq. 7), the higher is the cementation exponent the higher is the sensitivity of the electrical resistivity values to changes in porosity (Ellis and Singer, 2007). The relatively similar m values that were obtained in the three layers indicate a similar sensitivity of the electrical resistivity values to the slight differences in porosity observed in the different layers.

Fig. 7. Images of the altered and fissured limestone formation taken while drilling the main well at the O-ZNS observatory.

Table 3. The Archie's petrophysical parameters obtained in the three layers of the model.

Layer	Depth (m)	a	m	n
1	6.61-9.00	0.80	1.60	2.00
2	9.01-14.00	0.70	1.60	2.00
3	14.01-19.00	0.60	1.47	2.00

The inversion results showed a value of 0.8 for the parameter a in layer 1, while it showed a value of 0.7 and 0.6 in layers 2 and 3 respectively. Even though no real correlation was found between this parameter and tortuosity or lithology, a is an empirical constant which is believed to have a role in the compensation for systematic errors in the porosity, electrical resistivity or pore fluid resistivity measurements (Glover, 2016, 2015). This empirical factor which appeared

in the Winsauer et al. (1952) modification of the Archie's first law usually provided improved fits with experimental data, especially when dealing with low-quality and sparse types of datasets. It is commonly assumed that the size of a is a measure of the extent to which an overall systematic error is present in the measurements. Recent research suggested that these errors produce non-unity values of a, while the closer this parameter is to unity, the better is the data quality. Additionally, a has an important role in the calculation of a more accurate m value, since it compensates for the experimental errors present in the parameters used to calculate m during the fitting procedure (Glover, 2016). Throughout the inversion, a takes the appropriate fitted value to compensate for the presence of systematic errors and reduce their effects on the obtained m value. Therefore, the value of a obtained from the fit can be considered as an empirical parameter that describes the accuracy of the measured data in the Archie equation. The observed decreasing behavior value of a, from 0.8 in layer 1 to 0.6 in layer 3 could be attributed to the increase in the measurements errors associated with the evolution of alteration, fracturation and karstification with depth. This phenomenon can increase the medium heterogeneities and produce errors in the field measurements which the fitted value of a compensated for during the inversion. Even though a was not shown to have an underlying physical meaning, few studies suggested a values ranging between 0.4 and 2.3 in the case of limestone formations (Timur et al., 1972; Porter and Carothers, 1970; Carothers, 1968). In accordance with our inversion results, the most recent studies reported values of a ranging between 0.2 and 1.8 for limestone formations (Glover, 2016, 2015).

The inversion of the CRIM showed a ε_s value of 7.99 in Layer 1, 7.97 in Layer 2 and 8.00 in Layer 3. ε_s is mainly influenced by the mineralogy and rock formation characteristics. Therefore, similar values were expected to be observed in the three layers, knowing that they are all considered as part of the limestone rock main geological unit (Table 1). However, the slight differences in the ε_s values observed in the three layers can be attributed to the differences

in the geological characteristics of the layers in terms of materials heterogeneity and degree of alteration which evolved with depth. Nevertheless, these slight differences, as small as they are, could also be simply induced by the mathematical procedure of the inversion. In accordance with our results, values ranging between 4 and 13 have been reported in the literature for the solid phase dielectric permittivity of limestone formations, which is considered as one of the main sources of uncertainties in the electromagnetic waves application of the CRIM model (Mount and Comas, 2014; Reynolds, 2011; Cassidy, 2009).

The inversion of the CRIM showed an α value of 0.50 in Layer 1, 0.58 in Layer 2 and 0.61 in Layer 3. Values ranging between -1 and 1 were reported for α over the last few decades, which is a geometrical factor connecting the effective layering direction of the components to the applied electric field direction (West et al., 2003; Knoll, 1996; Roth et al., 1990). Several GPR studies indicated that most geological facies can take an α value of 0.5 (West et al., 2003; Knoll, 1996). Values ranging between 0.46 and 0.65 have been previously obtained during laboratory measurements (Mount and Comas, 2014; Moysey and knight, 2004).

Table 4. The CRIM's petrophysical parameters obtained in the model layers.

Layer	Depth (m)	α	ε_s
1	6.61-9.00	0.50	7.99
2	9.01-14.00	0.58	7.97
3	14.01-19.00	0.61	8.00

This approach was shown to produce acceptable results reflected in a very good fit between the measured and calculated data in the three layers, and with values that generally fall in the ranges reported in previous studies. The degree of accuracy of this approach is defined by the resolution of the hydrogeological model and its capability in capturing the VZ water content variations. The water content distribution is strongly influenced by the extent of heterogeneities incorporated in the hydrogeological model and in the porosity parameter of the empirical

relationships, especially in limestone formations with complex porosity patterns. Characterizing the impact of the observed fissures and fractures networks on the water flow at the field scale of the O-ZNS VZ is indeed crucial. Therefore, our future work is focused on the development of a precise description of the water flow through the whole porosity of this highly heterogeneous VZ by combining 3D experimental observations and numerical simulations with dual-porosity or dual-permeability approaches. This will form the basis to incorporate the complex multiple porosity patterns in the petrophysical relationships in order to provide an improved estimation of petrophysical parameters. The geological heterogeneities encountered at different study sites might explain the wide range of values reported in the literature for the Archie's and CRIM's parameters, especially in carbonate geology environments, which are complex mediums that can develop different porosity patterns, fractures networks and flow paths.

6. Conclusion

This study attempted to investigate the relationship between geophysical properties and water content distribution, and determine the Archie's and CRIM's petrophysical parameters by integrating ER and dielectric permittivity data with simulated water content data at the scale of a highly heterogeneous limestone VZ. The simulated and experimental hydrogeological data displayed a very good correspondence with the geophysical data reflected in coherent variations in water content, ER and relativity permittivity. These observations showed a significant sensibility of geophysical methods to water content variations, and demonstrated the potential of these methods in investigating hydrogeological processes at our study site.

The inversion results of the Archie model showed values ranging between 0.6 and 0.8 for a and between 1.47 and 1.60 for m. On the other hand, the inversion results of the CRIM showed values ranging between 0.50 and 0.61 for α and between 7.97 and 8.00 for ε_s. Similar results

549 were obtained in the three model layers, with slight differences that were attributed to the
550 vertical heterogeneities of the limestone rock formation (e.g., degree of alteration, fracturation,
551 karstification). This observation demonstrates the sensitivity of petrophysical parameters to
552 vertical geological heterogeneities that should be taken into account when calculating these
553 parameters. Given the ranges of variability used in the inversion, the obtained values are within
554 the bounds of values found in the literature, where a wide range have been reported for
555 carbonate formations due to their complex geological features that might vary greatly among
556 different study sites.

557 Throughout this study, the petrophysical parameters were successfully obtained with a very
558 good fit between the measured and simulated data. However, the demonstrated approach
559 showed an important sensitivity to the resolution of water content variations captured by the
560 used hydrogeological model, and to the geological heterogeneities of the medium. Therefore,
561 the perspectives include further improvements to this approach by conducting extensive studies
562 at larger scales, and combining 3D experimental observations and numerical simulations using
563 dual-porosity and dual-permeability modeling approaches that can capture the water content
564 and geological heterogeneities at a higher resolution in complex and fractured limestone
565 formations. In this context, our future work is focused on the development of a geological model
566 constrained by laboratory calibrations that can give a better estimation of the limestone complex
567 porosity patterns to be incorporated in the hydrogeological model and empirical relationships.

568 ## Acknowledgment

569 This study was conducted within the framework of the O-ZNS project which is part of the
570 PIVOTS program (https://plateformes-pivots.eu/o-zns/?lang=en). We gratefully acknowledge
571 the financial support provided to the PIVOTS project by the Région Centre–Val de Loire (ARD
572 2020 program and CPER 2015-2020), and by the French Ministry of Higher Education and

Research. This research work is co-funded by the Labex Voltaire (ANR-10-LABX-100-01) and by the European Union with the European Regional Development Fund (FEDER) in Centre-Val de Loire. Data can be obtained upon request to the corresponding author. In addition, the data will be soon available on an O-ZNS data repository with their own DOI.

References

Abbar, B., Isch, A., Michel, K., Abbas, M., Vincent, H., Abbasimaedeh, P., & Azaroual, M. (2021). Fiber optic technology for environmental monitoring: state of the art and application in the observatory of transfers in the vadose zone (O-ZNS). Chapter book in "Instrumentation and Measurement Technologies for Water Cycle Management", Springer (Wiley). https://link.springer.com/book/9783031082610.

Abbas, M., Jardani, A., Soueid Ahmed, A., Revil, A., Brigaud, L., Bégassat, Ph., & Dupon, J. P. (2017). Redox potential distribution of an organic-rich contaminated site obtained by the inversion of self-potential data. Journal of Hydrology. 554,111–127. https://doi.org/10.1016/j.jhydrol.2017.08.053.

Ahmed, A. S., Jardani, A., Revil, A., & Dupont, J. P. (2014). Hydraulic conductivity field characterization from the joint inversion of hydraulic heads and self-potential data. Water Resources Research . 50, 3502–3522. https://doi.org/10.1002/2013WR014645.

Aldana, C., Isch, A., Bruand, A., Azaroual, M., & Coquet., Y. (2021). Relationship between hydraulic properties and material features in a heterogeneous vadose zone of a vulnerable limestone aquifer. Vadose Zone Journal. e20127. https://doi.org/10.1002/vadose zonej2.20127.

Ammar, A. & Kamal, K. A. (2017). Resistivity method contribution in determining of fault zone and hydro-geophysical characteristics of carbonate aquifer, eastern desert, Egypt. Applied Water Science. https://doi.org/10.1007/s13201-017-0639-9.

Archie, G. E. (1942). The electrical resistivity log as an aid in determining some reservoir characteristics. Transactions of American Institute of Mining Metallurgical Engineers. 146. 54-62. https://doi.org/10.2118/942054-G.

600 Arora, B., Dwivedi, D., Faybishenko, B., Jana, R., & Wainwright, H. (2019). Understanding
601 and Predicting Vadose Zone Processes. Reviews in Mineralogy, 85.
602 https://doi.org/10.1515/9781501512001-011.

603 Birchak, J. R., Gardner, C. G., Hipp, J. E., & Victor, J. M. (1974). High dielectric constant
604 microwave probes for sensing soil moisture. IEEE, 62: 93-98. doi:
605 10.1109/PROC.1974.9388.

606 Binley, A., Winship, P., Middleton, R., Pokar, M., & West, J. (2001). High-resolution
607 characterization of vadose zone dynamics using crossborehole radar. Water Resources
608 Research. 37(11), 2639–2652. https://doi.org/10.1029/2000WR000089.

609 Binley, A., Cassiani, G., Middleton, R., & Winship, P. (2002a). Vadose zone flow model
610 parameterisation using cross-borehole radar and resistivity imaging. Jornal of
611 Hydrology. 267:147–159. https://doi.org/10.1016/S0022-1694(02)00146-4.

612 Binley, A., Cassiani, G., & Deiana, R. (2010). Hydrogeophysics - Opportunities and
613 Challenges. Bollettino di Geofisica Teorica ed Applicata,. 51. 267-284.

614 Binley, A., Hubbard, S. S., Huisman, J. A., Revil, A., Robinson, D. A., Singha, K., & Slater, L.
615 D. (2015). The emergence of hydrogeophysics for improved understanding of
616 subsurface processes over multiple scales. Water Resources Research. 51. 3837–3866.
617 https://doi.org/10.1002/2015WR017016.

618 Blazevic, L., Bodet, L., Pasquet, S., Linde, N., Jougnot, D., Longuevergne, L. (2020). Time-
619 Lapse Seismic and Electrical Monitoring of the Vadose Zone during A Controlled
620 Infiltration Experiment at the Ploemeur Hydrological Observatory, France. Water. 12.
621 10.3390/w12051230.

622 Brunet, P., Clément, R., & Bouvier, C. (2010). Monitoring soil water content and deficit using
623 Electrical Resistivity Tomography (ERT) – A case study in the Cevennes area, France.
624 Journal of Hydrology, 380. 146-153. https://doi.org/10.1016/j.jhydrol.2009.10.032.

625 Buchner, R., Barthel, J., & Stauber, J. (1999). The dielectric relaxation of water between 0°C
626 and 35°C. Chemical Physics Letters. 306(1–2), 57– 63. https://doi.org/10.1016/S0009-
627 2614(99)00455-8.

628 Carothers, J. E. (1968). A statistical study of the formation factor relation. The Log Analyst 9
629 (5). 13-20 .

630 Cassiani, G., Ferraris, S., Giustiniani, M., Deiana, R., & Strobbia, C. (2009b). Time-lapse
631 surface-to-surface GPR measurements to monitor a controlled infiltration experiment.
632 Bollettino di Geofisica Teorica ed Applicata. 50. 209-226.

633 Cassidy, N. (2009). Ground Penetrating Radar Data Processing, Modelling and Analysis.
634 https://doi.org/10.1016/B978-0-444-53348-7.00005-3.

635 Chan, C. Y., & Knight; R. J. (2001). Laboratory measurements of electromagnetic wave
636 velocity in layered sands, Water Resources Research, 37(4), 1099–1105,
637 doi:10.1029/2000WR900356.

638 Chan, C. Y., & Knight; R. J. (1999). Determining water content and saturation from dielectric
639 measurements in layered materials. Water Resources Research. 35. 85-93.
640 doi/pdf/10.1029/1998WR900039.

641 Dafflon, B., Irving, J., & Barrash, W. (2011). Inversion of multiple intersecting high-resolution
642 crosshole GPR profiles for hydrological characterization at the Boise hydrogeophysical
643 research site. Journal of Applied Geophysics. 73:305–314.
644 https://doi.org/10.1016/j.jappgeo.2011.02.001.

645 De Jong, S., Heijenk, R., Nijland, W., & Meijde, M. (2020). Monitoring Soil Moisture
646 Dynamics Using Electrical Resistivity Tomography under Homogeneous Field
647 Conditions. Sensors (Basel, Switzerland). 20(18). 5313. https://doi.org/ 20.
648 10.3390/s20185313.

649 Eching, S. O., Hopmans, J. W., & Wendroth, O. (1994). Unsaturated hydraulic conductivity
650 from transient multistep outflow and soil water pressure data. Soil science society of
651 America journal 58(3): 687–695.

652 Ellis, D. V., & Singer, J. M. (2007). Well Logging for Earth Scientists. Vol. 692, Springer,
653 Dordrecht.

654 Evett, S. (2003). Soil Water Measurement by Time Domain Reflectometry. In Encyclopedia of
655 Water Science; Marcel Dekker, Inc.: New York, NY, USA; ISBN 0-8247-4241-9.

656 Evett, S. (2008). Neutron moisture meters. Field Estimation of Soil Water Content: A Practical
657 Guide to Methods, Instrumentation, and Sensor Technology. 39-54. ISSN 1018–5518.

658 Gardner, W. R. (1956). Calculation of Capillary Conductivity from Pressure Plate Outflow
659 Data. 317–320p.

Garré, S., Hyndman, D., Mary, B., and Werban, U. (2021). Geophysics conquering new territories: The rise of Agrogeophysics. Vadose Zone Journal. p. e20115. https://doi.org/10.1002/vzj2.20115.

Gance, J., Malet, J. P., Supper, R., Sailhac, P., Ottowitz, D., & Jochum, B. (2016). Permanent electrical resistivity measurements for monitoring water circulation in clayey landslides. Journal of Applied Geophysics. 126, 28-115. https://doi.org/10.1016/j.jappgeo.2016.01.011.

Glover, P. W. J., Gomez, J. B., Meredith, P. G., Hayashi, K., Sammonds, P. R., & Murrell, S. A. F. (1997). Damage of saturated rocks undergoing triaxial deformation using complex electrical conductivity measurements: experimental results: Physics and Chemistry of the Earth, 22, no. 1–2, 57–61. doi: 10.1016/S0079-19469700078-5.

Glover, P. W. J. (2009). What is the cementation exponent? A new interpretation. The Leading Edge, 28, 82–85. https://doi.org/10.1190/1.3064150.

Glover, P. W. J. (2010). A generalised Archie's law for n phases. Geophysics. 75, E247–E265. https://doi.org/10.1190/1.3509781, 2010.

Glover, P. W. J. (2015). Geophysical properties of the near surface Earth: Electrical properties. Treatise on Geophysics, 11, 89–137, 2015. https://doi: 10.1016/B978-0-444-53802-4.00189-5.

Glover, P. (2016). Archie's law – a reappraisal: Solid Earth. 7. 1157-1169. https://doi.org/10.5194/se-7-1157-2016.

Glover, P. W. J. (2017). A new theoretical interpretation of Archie's saturation exponent. Solid Earth. 8. 805-816. https://doi.org/10.5194/se-8-805-2017.

Griffiths, D. H., Barker, R. D. (1993). Two-dimensional resistivity imaging and modeling in areas of complex geology. Journal of Applied Geophysics. 29. 211–226.

Hagrey, S. (2007). Geophysical imaging of root-zone, trunk, and moisture heterogeneity. Journal of experimental botany. 58. 839-54. https://doi.org/10.1093/jxb/erl237.

He, H., Aogu, K., Li, M., Xu, J., Sheng, W., Jones, S.B., González-Teruel, J.D., Robinson, D.A., Horton, R., Bristow, K., Dyck, M., Filipović, V., Noborio, K., Wu, Q., Jin, H., Feng, H., Si, B., & Lv, J. (2021). Chapter Three - A review of time domain reflectometry

(TDR) applications in porous media. In: D.L. Sparks (Ed.). Advances in Agronomy. Academic Press. 83-155. https://doi.org/10.1016/bs.agron.2021.02.003.

Hendrickx, J. M. H., Das, B., Corwin, D. L., Wraith, J. M., & Kachanoski, R. G. (2002). Relationship between soil water solute concentration and apparent soil electrical conductivity. In Dane, J. H., Topp, G.C. (Eds.), Methods of Soil Analysis: Part 4. Physical Methods. Soil Science Society of America, Madison, WI, USA. 1275–1282.

Herkelrath, W. N., Hamburg, S. P., & Murphy, F. (1991). Auto- matic, real-time monitoring of soil moisture in a remote field area with time domain re- flectometry. Water Resources Research. 2T, 857- 864.

Hill, H. J., & Milburn, J. D. (1956). Effect of clay and water salinity on electrochemical behaviour of reservoir rocks. Petroleum Transactions. 207. 65–72. https://doi.org/10.2118/532-G.

Hubbard, S. S., Chen, J. S., Peterson, J., Majer, E. L., Williams, K., Swift, D. J., Mailloux, B., & Rubin, Y. (2001a). Hydrogeological characterization of the South Oyster Bacterial Transport Site using geophysical data. Water Resources Research. 37(10). 2431–2456. https://doi.org/10.1029/2001WR000279.

Huisman, J. A., Hubbard, S. S., Redman, J. D., & Annan, P. A. (2003), Measuring soil water content with ground penetrating radar: A review. Vadose Zone Jornal. 2(4). 476–491. https://doi.org/10.2113/2.4.476.

Isch, A., Montenach, D., Hammel, F., Ackerer, P., Coquet, Y (2019). A Comparative Study of Water and Bromide Transport in a Bare Loam Soil Using Lysimeters and Field Plots. Water. 11. 1199. https://doi.org/10.3390/w11061199.

Isch, A., Coquet, Y., Abbar, B., Aldana, B., Abbas, M., Bruand, A., Azaroual, M. (2022). A comprehensive experimental and numerical analysis of water flow and travel time in a highly heterogeneous vadose zone. Journal of Hydrology. 610. 127875. https://doi.org/10.1016/j.jhydrol.2022.127875.

Jardani, A., Revil, A., & Dupont, J. P. (2012). Stochastic joint inversion of hydrogeophysical data for salt tracer test monitoring and hydraulic conductivity imaging. Advances in Water Resources. 52. 62-77. https://doi.org/10.1016/j.advwatres.2012.08.005.

Johnson, T. C., Versteeg, R. J., Ward, A., Day-Lewis, F. D., & Revil, A. (2010). Improved hydrogeophysical characterization and monitoring through parallel modeling and

720 inversion of time-domain resistivity and induced-polarization data. Geophysics. 75. 27-
721 41. https://doi.org/10.1190/1.3475513.

722 Johnson, T., Versteeg, R., Thomle, J., Hammond, G., Chen, X., & Zachara, J. (2015). Four-
723 dimensional electrical conductivity monitoring of stage-driven river water intrusion:
724 Accounting for water table effects using a transient mesh boundary and conditional
725 inversion constraints. Water Resources Research.51. 6177–6196.
726 https://doi.org/10.1002/2014WR016129.

727 Klotzsche, A., Jonard, F., Looms, M. C., Van Der Kruk, J., & Huisman, J. A. (2018). Measuring
728 soil water content with ground penetrating radar: A decade of progress. Vadose Zone
729 Jornal. 17:180052. https://doi.org/10.2136/vadose zonej2018.03.0052.

730 Klotzsche, A., L ¨arm, L., Vanderborght, J., Cai, G., Morandage, S., Z ¨orner, M. (2019).
731 Monitoring soil water content using time lapse horizontal borehole GPR data at the field
732 plotscale. Vadose Zone Journal. 18. 190044. https://doi.org/10.2136/vzj2019.05.0044.

733 Klotzsche, A., Van Der Kruk, J., Linde, N., Doetsch, J., & Vereecken, H. (2013). 3-D
734 characterization of high-permeability zones in a gravel aquifer using 2-D crosshole GPR
735 full-waveform inversion and wave guide detection. Geophysical Journal International.
736 195:932–944. https://doi.org/10.1093/gji/ggt275.

737 Kowalsky, M., Finsterle, S., Peterson, J., Hubbard, S., Rubin, Y., Majer, E., Ward, A., & Gee,
738 G. (2005). Estimation of field-scale soil hydraulic and dielectric parameters through
739 joint inversion of GPR and hydrological data. Water Resources Research., 41, W11425,
740 https://doi.org/10.1029/2005WR004237.

741 Linde, N., Binley, A., Tryggvason, A., Pedersen, L. B., & Revil, A. (2006). Improved hydro-
742 geophysical characterization using joint inversion of cross-hole electrical resistance and
743 ground-penetrating radar traveltime data. Water Resources Research. 42. W12404.
744 https://doi.org/10.1029/2006WR005131.

745 Looms, M. C., Binley, A., Jensen, K. H., Nielsen, L., & Hansen, T. M. (2008a). Identifying
746 unsaturated hydraulic parameters using an integrated data fusion approach on cross-
747 borehole geophysical data. Vadose Zone Jornal. 7. 238–248.
748 https://doi.org/10.2136/vadose zonej2007.0087.

749 Looms, M. C., Jensen, K. H., Binley, A., & Nielsen, L. (2008b). Monitoring Unsaturated Flow
750 and Transport Using Cross-Borehole Geophysical Methods. Vadose Zone Jornal. 7.
751 227–237. https://doi.org/10.2136/vadose zonej2007.0087.

752 Lucia, F. J. (2007). Carbonate Reservoir Characterization: An Integrated Approach. Springer.
753 https://link.springer.com/book/10.1007/978-3-540-72742-2

754 Lunt, I., Hubbard, S. S., & Rubin, Y. (2005). Soil moisture estimation using ground-penetrating
755 radar reflection data. Journal of Hydrology. 307. 254–269.
756 https://doi.org/10.1016/j.jhydrol.2004.10.014.

757 Mallet, C., Isch, A., Laurent, G., Jodry, C., Azaroual, M. (2022). Integrated static and dynamic
758 geophysical and geomechanical data for characterization of transport properties.
759 International Journal of Rock Mechanics and Mining Sciences. 153.
760 https://doi.org/10.1016/j.ijrmms.2022.105050.

761 Mallet, C., Jodry, C., Isch, A., Laurent, G., Deparis, J. & Azaroual, M. (2021). Multi-
762 geophysical field measurements to characterize lithological and hydraulic properties of
763 a multi-scale karstic and fractured limestone vadose zone: Beauce aquifer (O-ZNS).
764 Chapter book in: Instrumentation and Measurement Technologies for Water Cycle
765 Management, Springer. https://link.springer.com/book/9783031082610.

766 Mary, B., Peruzzo, L., Boaga, J., Schmutz, M., Wu, Y., Hubbard, S., & Cassiani, G. (2018).
767 Small scale characterization of vine plant root water uptake via 3D electrical resistivity
768 tomography and Mise-à-la-Masse method. Hydrology and Earth System Sciences. 22.
769 5427-5444. https://doi.org/10.5194/hess-22-5427-2018.

770 Mohamed, A., & Hamada, G. (2017). Determination Techniques of Archie's Parameters: a, m
771 and n in Heterogeneous Reservoirs. Journal of Geophysics and Engineering. 14.
772 https://doi.org/10.1088/1742-2140/aa805c.

773 Mount, G. J., & Comas, X. (2014). Estimating porosity and solid dielectric permittivity in the
774 Miami Limestone using high-frequency ground penetrating radar (GPR) measurements
775 at the laboratory scale. Water Resources Research. 50, 7590–7605.
776 https://doi.org/10.1002/ 2013WR014947.

777 Mualem, Y. (1976.) A new model for predicting the hydraulic conductivity of unsaturated
778 porous media. Water Resources Research. 12(3. 513–522.
779 https://doi.org/10.1029/WR012i003p00513.

780 Moysey, S., & Knight, R. J. (2004). Modeling the field-scale relationship between dielectric
781 constant and water content in heterogeneous systems. Water Resources Research.40.
782 W03510, doi:10.1029/2003WR002589.

783 Nimmo, J. R. (2005). Unsaturated Zone Flow Processes. Encyclopedia of Hydrological
784 Sciences, Wiley, Chichester, UK. 2299–2322.

785 Knoll, M. D., (1996). A petrophysical basis for Ground-penetrating radar and very early time
786 electromagnetics, electrical properties of sand-clay mixtures. Unpublished Ph.D.
787 dissertation, University of British Columbia, 316 p.

788 Paz, C., Alcala, F. J., Carvalho, J. M., & Ribeiro, L. (2017). Current uses of ground penetrating
789 radar in groundwater-dependent ecosystems research. Science of The Total
790 Environment., 595. 868–885. https://doi.org/10.1016/j.scitotenv.2017.03.210.

791 Porter, C. R. & Carothers, J. E. (1970). Formation factor porosity relation derived from well
792 log data, Trans. SPWLA 11th Ann. Logging Symp., 1–19, 1970.

793 Reynolds, J. (2011). An Introduction to Applied and Environmental Geophysics. Wiley. ISBN:
794 978-0-471-48535-3.

795 Richards, L.A., 1931. Capillary conduction of liquids through porous mediums. J. Appl. Phys.
796 1, 318–333. https://doi.org/10.1063/1.1745010.

797 Robinson, D., Jones, S., Wraith, J., Or, D., & Friedman, S. (2003). A review of advances in
798 dielectric and electrical conductivity measurement in soils using time domain
799 reflectometry, Vadose Zone Jornal. 2. 444–475. https://doi.org/10.2113/2.4.444.

800 Robinson, D., Binley, A., Crook, N., Day-Lewis, F., Ferré, T., Grauch, V.J.S, Knight, R., Knoll,
801 M., Lakshmi, V., Miller, R., Nyquist, J., Pellerin, L., Singha, K., & Slater, L. (2008).
802 Advancing process-based watershed hydrological research using near-surface
803 geophysics: A vision for, and review of, electrical and magnetic geophysical methods.
804 Hydrological Processes – Wiley. 22. 3604–3635. https://doi.org/10.1002/hyp.6963.

805 Roth, K., Schulin, R., Fluhler, H., & Attinger, W. (1990). Calibration of time domain
806 reflectometry for water content measurement using a composite dielectric approach.
807 Water Resources Research. 26. 2267–2273.
808 https://doi.org/10.1029/WR026i010p02267.

809 Rubin, Y., & Hubbard, S. S. (2005). Hydrogeophysics, 523 pp., Springer, N. Y.

Rust, C. F. (1952). Electrical Resistivity Measurements on Reservoir Rock Samples bv the Two-Electrode and Four-Electrode Methods. AIME Transactions, 195. 217-224.

Schön, J. H. (2004). Physical Properties of Rocks: Fundamentals and Principles of Petrophysics. Edited by: Helbig, K. and Treitel, S., Vol.18, Amsterdam, the Netherlands: Elsevier, ISBN: 008044346X, 2004.

Šimůnek, J., van Genuchten, M.T., & Šejna, M. (2016). Recent Developments and Applications of the HYDRUS Computer Software Packages. Vadose Zone Journal. 15(7). https://doi.org/10.2136/vadose zonej2016.04.0033.

Skierucha, W., Wilczek, A., Szypłowska, A., Sławiński, C., Lamorski, K., Skierucha, W., Wilczek, A., Szypłowska, A., Sławiński, C., & Lamorski, K. (2012). A TDR-based soil moisture monitoring system with simultaneous measurement of soil temperature and electrical conductivity. Sensors, 12. 13545–13566. https://doi.org/10.3390/s121013545.

Steelman, C., & Endres, A. (2011). Comparison of Petrophysical Relationships for Soil Moisture Estimation using GPR Ground Waves. Vadose Zone Journal. 10. 270. https://doi.org/10.2136/vadose zonej2010.0040.

Stephens, D. B. (2019). Vadose Zone Hydrology. CRC Press, 347 Pages. ISBN 9780367448783.

Sweeney, S. A. & Jennings, H. Y. (1960). The electrical resistivity of preferentially water-wet and preferentially oil-wet carbonate rock. Producers Monthly. 24 (7). 29-32, 1960.

Tiab, D., & Donaldson, E. C. (2004). Petrophysics: Theory and Practice of Measuring Reservoir Rock and Fluid Transport Properties: Second Edition. Gulf Professional Publishing – Elsevier. ISBN: 9780080497655

Timur, A., Hemkins, W. B., & Worthington, A. E. (1972). Porosity and pressure dependence of formation resistivity factor for sandstones. Trans. CWLS 4th Formation Evaluation Symp., 30 pp.

Topp, G. C., Davis, J. L., & Annan, A. P. (1980). Electromagnetic determination of soil water content: Measurements in coaxial transmission lines. Water Resources Research. 16.574–582. https://doi.org/10.1029/WR016i003p00574.

van Genuchten, M. T. (1980). A closed-form equation for predicting the hydraulic conductivity of unsaturated soils. Soil Science Society of America Journal. 44(5). 892–898. https://doi.org/10.2136/sssaj1980.03615995004400050002x.

van Genuchten, M. T., Leij, F. J., & Yates, S. R. (1991). The RetC code for quantifying hydraulic functions of unsaturated soils. EPA/600/2-91/065, R.S. 83.

Verhoef, A., Fernández-Gálvez, J., Diaz-Espejo, A., Main, B.E. & El-Bishti, M. (2006). The diurnal course of soil moisture as measured by various dielectric sensors: Effects of soil temperature and the implications for evaporation estimates. Journal of Hydrology. 321. 147-162. https://doi.org/10.1016/j.jhydrol.2005.07.039.

Vereecken, H., Binley, A., Cassiani, G., Revil, A., & Titov, K. (2006). Applied Hydrogeophysics, 383 pp., Springer, Dordrecht, Netherlands.

Vilhelmsen, T. N., Behroozmand, A. A., Christensen, S. & Nielsen, T. H. (2014). Joint inversion of aquifer test, MRS, and TEM data. Water Resources Research. 50. 3956–3975. https://doi.org/10.1002/2013WR014679.

Wehrer, M., & Slater, L. (2015). Characterization of water content dynamics and tracer breakthrough by 3-D electrical resistivity tomography (ERT) under transient unsaturated conditions. Water Resources Research. 51. https://doi.org/10.1002/2014WR016131.

West, L. J., Huang, Y., & Handley, K. (2001). Dependence of Sandstone Dielectric Behaviour on Moisture Content and Lithology. Proceedings of the Symposium on Applications of Geophysics to Engineering and Environmental Problems (SAGEEP2001), Environmental and Engineering Geophysical Society, Denver, CO. https://doi.org/10.4133/1.2922904.

West, L. J., Handley, K., Huang, Y., & Pokar, M. (2003). Radar frequency dielectric dispersion in sandstone: Implications for determination of moisture and clay content. Water Resources Research, 39.2. https://doi.org/10.1029/2001WR000923.

Winsauer, W. O., Shearin, H. M., Masson, P. H., & Williams, M. (1952). Resistivity of brine-saturated sands in relation to pore geometry. AAPG Bull., 36, 253–277. https://doi.org/10.1306/3D9343F4-16B1-11D7-8645000102C1865D.

867 Worthington, P. F. (1993). The uses and abuses of the Archie equations, 1: The formation
868 factor-porosity relationship. Journal of Applied Geophysics., 30, 215–228.
869 https://doi.org/10.1016/0926-9851(93)90028-W.

870 Yaramanci, U. (2000). Geoelectric exploration and monitoring in rock salt for the safety
871 assessment of underground waste disposal sites. Journal of Applied Geophysics., 44,
872 181–196.

873

874

875 **Table 5.** (a) Description of the samples considered for the representation of the VZ profile and
876 the simulation of water flow with HYDRUS-1D: depth, description, saturated water content (θ_s
877), experimental saturated water content ($\theta_{sExp.}$), hydraulic conductivity (K_s), α, and n.

Geological Unit	Depth (m)	Sample	Description	θ_s (cm3/cm3)	$\theta_{s\ Exp.}$ (cm^3/cm^3)	K_s (cm/d)	α cm^{-1}	n (/)
1	0.00-0.30	S_A	Soil	0.4735	0.4864	30.24	0.0242	1.15
	0.31-0.60	S_B	Soil	0.4661	0.4612	53.57	0.0242	1.16
	0.61-0.90	S_C	Soil	0.5002	0.4162	47.52	0.0366	1.16
2	0.91-1.30	P_A	Powdery limestone	0.4511	0.4230	7.31	0.0247	1.17
	1.30-3.50	P_B	Powdery limestone	0.3659	0.3525	0.455	0.0073	1.25
	3.51-4.10	I_A	Calcareous sand	0.3918	0.3775	35.22	0.0715	1.20
	4.11-4.60	P_C	Powdery limestone	0.2969	0.3080	0.143	0.0031	1.22
	4.61-4.90	I_B	Calcareous sand	0.3698	0.4336	285.49	0.1600	1.23
	4.91-5.20	R_A	Altered rock	0.2984	0.3400	5000	0.5156	1.36
	5.21-5.50	I_B	Calcareous sand	0.3698	0.4336	285.49	0.1600	1.23
	5.51-6.60	P_D	Powdery limestone	0.3527	0.3491	0.185	0.0040	1.22
3	6.61-9.00	R_B	Massive rock	0.1547	0.1499	1.32	0.0150	1.16
	9.01-11.20	R_D	Massive rock	0.0949	0.1180	0.402	0.0096	1.17
	11.21-11.40	R_C	Massive rock	0.0504	0.0491	0.0097	0.0014	1.23
	11.41-14.00	R_D	Massive rock	0.0949	0.1180	0.402	0.0096	1.17
	14.01-16.00	R_E	Massive rock	0.1172	0.1333	500	0.1266	1.15

	16.01-19.00	R_F	Massive rock	0.1452	0.1639	500	0.1371	1.19

878

879

880

881

882

883 **Table 6** : The ranges of the Archie (a, m and n) and CRIM (α and ε_s) parameters used for the

884 inversion and those commonly reported in the literature for limestone formations.

Model	Parameter	Literature (limestone)	Inversion
Archie	a	$0.2 \leq a \leq 2.3$	$0.1 \leq a \leq 10$
	m	$1.6 \leq m \leq 3$	$1.0 \leq m \leq 10$
	n	$1.5 \leq n \leq 2.5$	$n = 2$
CRIM	α	$-1 \leq \alpha \leq 1$	$-1 \leq \alpha \leq 1$
	ε_s	$4 \leq \varepsilon_s \leq 11$	$1 \leq \varepsilon_s \leq 20$

885

886

887

888

889

890

891

892

893

894

895

896

897

898

899

Table 7. The Archie's petrophysical parameters obtained in the three layers of the model.

Layer	Depth (m)	a	m	n
1	6.61-9.00	0.80	1.60	2.00
2	9.01-14.00	0.70	1.60	2.00
3	14.01-19.00	0.60	1.47	2.00

922

923

924 **Table 8.** The CRIM's petrophysical parameters obtained in the model layers.

Layer	Depth (m)	α	ε_s
1	6.61-9.00	0.50	7.99
2	9.01-14.00	0.58	7.97
3	14.01-19.00	0.61	8.00

925

926